DEPARTMENT OF CHEMISTRY

Sydney Schuster

How I Wrote My Prospectus

The general shape of my prospectus was formed via conversations with my advisor. By the summer after my first year I had a general sketch of what I wanted to work on during my PhD. I then started data collection in earnest. This was for both my preliminary data for the prospectus and a publication. Going through the publication process really helped me refine my ideas, write a strong introduction and finalize preliminary data. Feedback from reviewers also helped direct my other aim. When the paper was submitted I went directly into adapting it into my prospectus. This required some significant additions but felt very accomplishable. My advisor read a mostly complete draft of my prospectus and provided feedback and also gave feedback on my oral presentation twice. This helped me streamline my ideas quite a bit. The full process of creating my prospectus took about 8 months including data collection and writing the publication. I probably spent 2-3 weeks on writing just the prospectus itself and then more time on the presentation and studying for the qualification exam.

Advice for Prospectus Writers

The biggest piece of advice I can give is to try not to stress about your prospectus. If you are in good communication with your advisor and they are happy with where your project is at you will be fine. I also recommend getting people who are not just your advisor, committee, or lab to read your drafts and provide feedback. The reviewers of our paper were so helpful in helping me think through potential pitfalls and friends reading the prospectus helped me make it much more intelligible. The graduate writing lab is a great resource to have a pair of trained eyes look it over!

Spatiotemporal visualization and structural characterization of cellular metabolism

Sydney O. Shuster

Committee:
Caitlin M. Davis, Ph.D. (advisor)
Elsa C. Yan, Ph.D.
Jason M. Crawford, Ph.D.

Date: March 17th, 2023
Time: 10:00 am
Location: YSB 302
Zoom link: https://bit.ly/3wbX0Gx

Specific Aims

Cellular metabolism is a complex network of enzymes and chemical reactions, finely tuned to meet the cell's energy needs. Recent research suggests that the cell regulates its metabolism not only through control of the activity of the enzymes involved, but also through exquisite spatial control of the components of metabolism in both membrane bound and membraneless organelles, the latter of which is formed via liquid-liquid phase separation (LLPS). Understanding how and why this spatial organization occurs is critical to understanding how metabolism adapts to stress and disease. Optical photothermal infrared microcopy (OPTIR) is a promising tool for investigating how proteins and metabolites organize themselves without need for bulky fluorescent labels and can also provide structural information on the proteins in the LLPS condensates. In this work, OPTIR will be applied to two disparate yet interconnected metabolic pathways, *de novo* lipogenesis (DNL) and glycolysis, to provide insight on how metabolism rearranges in stress and disease.

Aim 1 Characterize rates of DNL across cell lines and changes in DNL rates and localization in response to stress and drugs

Goal: Develop straightforward process for tracking rates of DNL in living cells and demonstrate usefulness in various disease models.

1.1) Optimize DNL rate measurements for Huh-7 cells.
1.2) Design a flow cell for real-time observation of drugs and stress on living cells.
1.3) Map basal DNL levels across cancer cells and create a library of DNL rates.
1.4) Measure the effects of drugs and stress on DNL towards the goal of understanding how drugs and stress conditions affect the disease state of DNL related conditions like non-alcoholic fatty liver disease (NAFLD) and metabolic syndrome.

Aim 2 Discern the changes in structure of phosphofructokinase (PFK) upon binding of allosteric effectors *in vitro* and *in cellulo*

Hypothesis: Binding of allosteric effectors will have widespread effects on PFK, causing filamentation in vitro and condensation in cells. Activators and inhibitors will produce different in vitro structures.

2.1) Express and purify high quality PFK using *E. coli* expression systems and nickel affinity purification.
2.2) Evaluate PFK isoform structures in solution and following filamentation/phase separation using circular dichroism, FTIR, OPTIR, and fluorescence spectroscopies.
2.3) Test conditions, including the addition of allosteric effectors and stressors like nutrient deprivation and anoxia, on cells to determine which conditions generate robust condensation. The morphology of the phase separation will be characterized using fluorescence microscopy.

Aim 3 Connect *in vitro* structures to *in cellulo* condensates

Hypothesis: Changes in the cellular environment affect the structure of PFK and different stressors and effectors produce different PFK structures even when condensate morphology is similar

3.1) Transfect cells with fluorescently labelled PFK and map basal and puncta forming conditions (i.e. allosteric effectors) with OPTIR to determine if overexpressed PFK can be visualized via IR imaging
3.2) Move to tag-free PFK to view the structures of puncta in OPTIR without the interference of bulky fluorescent tags. If PFK is difficult to locate without any label, small IR tags like azide modified amino acids can be used.
3.3) Study native stress conditions by employing THP-1 immune cells, which express PFK and have both inflammatory and anti-inflammatory states thought to affect PFK localization and structure through upregulation of allosteric effectors like citrate

Background and Significance

Modern cell biology and biochemistry has demonstrated the cell is not a 'well mixed' environment.[1] Instead, both membrane-bound organelles and membraneless assemblies serve to organize the cell and promote necessary chemistry in a dynamic and responsive fashion. Membraneless assemblies are driven primarily through liquid-liquid phase-separation (LLPS), in which many transient interactions cause the concentration of a solute into a separate phase.[2] Recently, the importance of membraneless metabolic assemblies in regulating processes like glycolysis has become apparent.[3] Glycolytic or G bodies, phase-separated condensates rich in glycolytic enzymes, substrates, and effectors, have been shown to be a key cellular response to stress. Glycolysis is not only a critical metabolic pathway for energy generation, it is also the first step in a variety of other metabolic processes including *de novo* lipogenesis (DNL). Further, glycolysis and DNL are classically upregulated in cancer (the Warburg effect) as the cell transitions away from aerobic metabolism.

In order to best understand cellular metabolism and how it changes in the disease state, metabolic networks must be studied with spatial and temporal resolution. This however, is not trivial, as traditional fluorescent labels can be difficult to incorporate and often alter the metabolic processes involved. Carbohydrates and lipids are much more difficult to label than proteins and fluorescently labelled analogs are often nonmetabolizable. Labeling with ^{13}C, however, has been shown to be nontoxic and nonperturbative to cells and is anabolized similarly to ^{12}C for molecules like glucose.[4] Isotopic labeling has been used to great success for diverse metabolic studies, including mass-spectrometry, but these methods lack spatial resolution within the cell.[4,5]

Vibrational microspectroscopy is a promising tool for studying metabolism in cells and organisms as it is a label-free and non-perturbative.[6–9] It can provide spatially and temporally resolved information on the identity of biomolecules in the cell as well as information on the secondary structure of protein molecules.[10] Additionally, when small vibrationally active probes such as azide, deuterium, or ^{13}C labels are used, vibrational microspectroscopy can inform on site-specific local environment and rates of metabolism across the cell.[11] For example, Li and Cheng used deuterium labeled glucose for tracking DNL in live cancer cells using stimulated Raman microspectroscopy (SRS).[12] However, their method could not also provide information on lipid identity and other surrounding biomolecules as it was single wavenumber based.

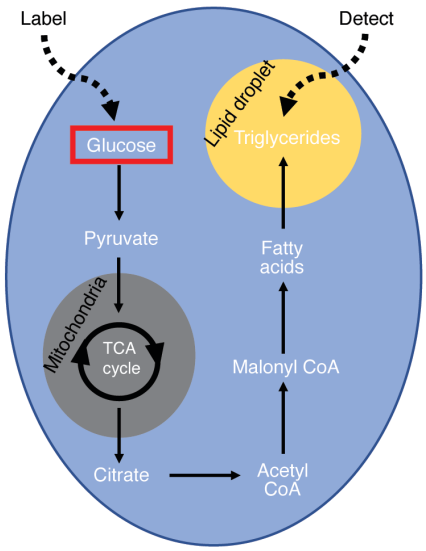

Figure 1. *De novo* lipogenesis

The two primary forms of vibrational spectroscopy used for cellular studies are FTIR and Raman spectroscopy. Unfortunately, both methods have significant drawbacks affecting in cell work. FTIR suffers from poor spatial resolution when used with microscopy.[13] This is because the diffraction limit of infrared light is orders of magnitude larger than that of visible light. Depending on the wavelength in question, FTIR has a spatial resolution ranging from ~3 μM to greater than 20 μM. This obscures all but the largest of cellular organelles and substructures. Additionally, FTIR cannot easily be performed in aqueous media, as water is a strong infrared absorber.[14,15] This means that work is usually done on cells that have been fixed and dried,[7,11,16] possibly disrupting the cellular environment as water is removed,[17] introducing artifacts such as Mie scattering,[18] and not allowing for real time, live cell tracking of cellular processes. Raman spectroscopy, on the other hand, has significantly less interference from water and can be performed on live cells.[12,16,17,19–21] The Raman cross-section, however, is small and signal intensity and signal to noise are consistent issues.[22] This leads to high laser powers and long collection times, which can damage cells.

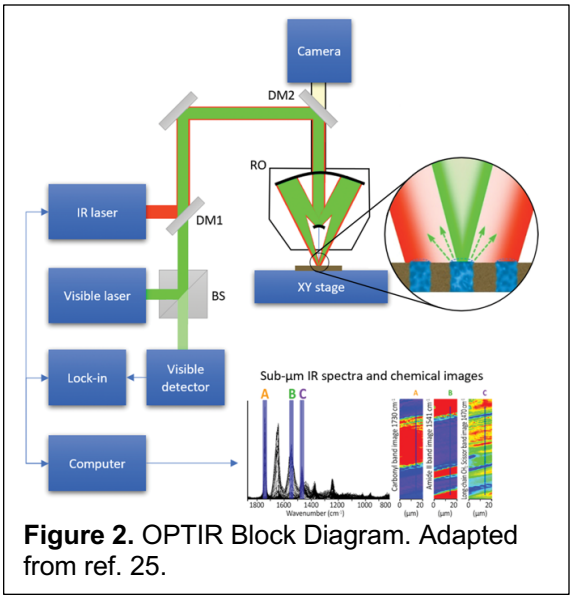

Figure 2. OPTIR Block Diagram. Adapted from ref. 25.

Optical photothermal infrared spectroscopy (OPTIR) was developed to address some of these issues.[20,23–25] It utilizes a pump-probe set-up in which a mid-IR laser 'pump' excites a spectral area, causing a photothermal response and expansion of the sample. A visible laser 'probe' detects changes in the refractive index of the sample caused by heating and transforms it into a mid-IR spectrum comparable to FTIR (Fig. 2).[26] The spectrometer is paired with a confocal or traditional light microscope, providing spatiotemporal control, and the technique is non-destructive and label-free. Since the diffraction limit of visible light is one to two orders of magnitude smaller than IR light this technique is 'super-resolution' IR-spectroscopy, providing IR spectra with a resolution of up to ~300 nm, equivalent to light microscopy.[27] This makes it incredibly well-suited for mapping structures within cells *in situ*. OPTIR can be used to both track cellular components through specific vibrational modes (i.e. lipid carbonyl stretching at 1747 cm^{-1}) and simultaneously report on protein secondary structure through deconvolution of the amide-I band (~1620-1670 cm^{-1}, with specific peaks correlating with secondary structural elements).[10,20] The technique has already been used to characterize both living and fixed cells[20], including identifying and analyzing the structure of aggregated amyloid protein in neurons.[28]

We aim to use OPTIR and vibrational probes as well as complementary techniques to elucidate nuances of cellular metabolism with high spatial, temporal, and spectral resolution. This project will examine glycolysis via the phase-separating and filament-forming properties of phosphofructokinase, liver isoform (PFKL) and DNL via tracking of the flow of carbons through the DNL pathway and its response to stress and disease conditions. This will provide important insight on how the cell organizes metabolism in health and disease and the methods developed will be applicable to studying a great variety of cellular processes.

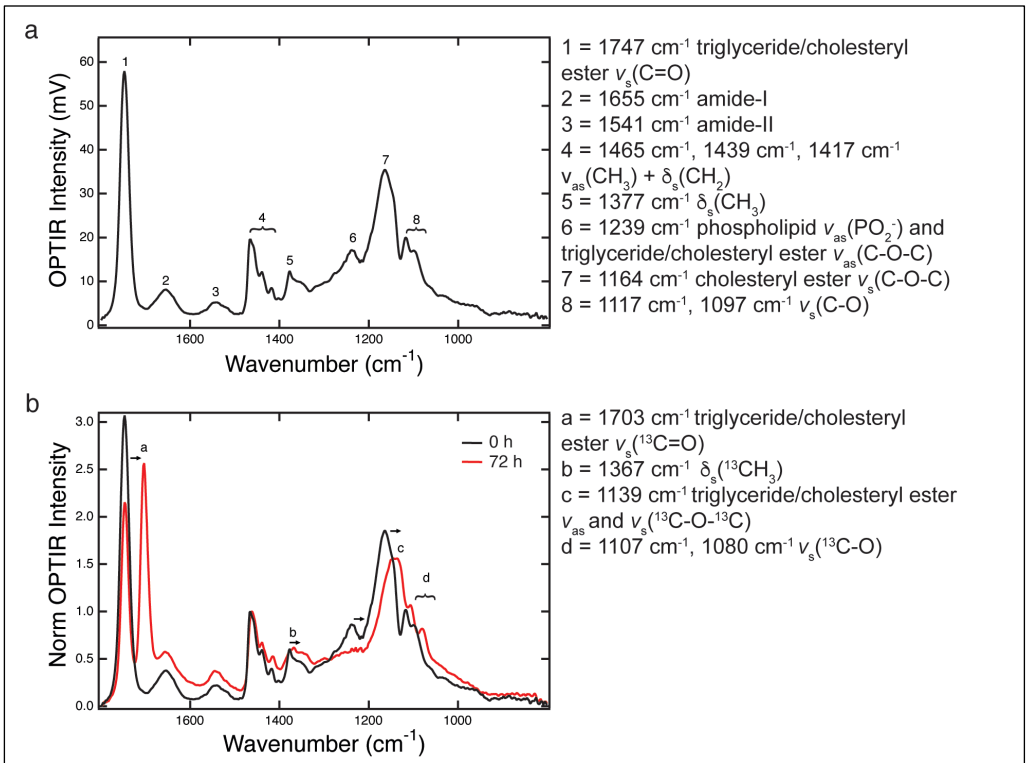

Figure 3. Peak assignments for ^{12}C and ^{13}C glucose fed 3T3-L1 adipocytes. (a) Representative OPTIR spectrum from a fixed, differentiated 3T3-L1 adipocyte with all peaks assigned. (b) Reprint of spectrum from (a) (black) overlaid with representative spectrum of differentiated 3T3-L1 adipocyte after 72 hour incubation with ^{13}C glucose. Peak shifts are indicated with arrows.

Preliminary Work

OPTIR has strong potential as a tool for resolving

metabolism in the cell, but it has never been used significantly beyond proof of concept for *in cellulo* studies as it was designed for materials chemistry. My preliminary worked has focused on optimizing OPTIR for biological samples and designing protocols for incorporation of small IR tags for in cell work. The preliminary data presented in this proposal develops a protocol of using OPTIR to assess rates of DNL in living and fixed cells utilizing cellular anabolism of ^{13}C labeled glucose. Figures and text have been reproduced in part from **Shuster, SO; Burke, MJ; Davis, CM, Spatiotemporal Heterogeneity of *De Novo* Lipogenesis in Fixed and Living Single-Cells** which is currently under revision.

In this work, we use OPTIR to investigate the rate of DNL in differentiated 3T3-L1 adipocytes. In DNL, glucose or other carbohydrates are metabolized to form free fatty acids (FFA) and triglycerides (Fig. 1).[29] The pathway begins with glycolysis. Pyruvate is then taken into the mitochondria and converted to citrate via the TCA cycle. Citrate is converted to acyl-CoA and malonyl-CoA which feed the fatty acid synthesis pathway and result in triglycerides. Triglycerides are then stored in lipid droplets as an energy reserve. By feeding cells ^{13}C labeled glucose in place of ^{12}C glucose, the ^{13}C progresses through the DNL pathway and labels the resulting lipids.[11]

^{13}C is a nonperturbative vibrational probe of *de novo* lipogenesis. To assess the power of OPTIR in resolving cellular components, the spatial and spectral resolution was evaluated using fixed 3T3-L1 cells. The cells were grown to confluency and differentiated using standard practices.[30] The resulting lipid droplet rich adipocyte cells were fixed. To limit background from water, a strong IR-absorber that overlaps significantly with the protein amide-I vibrational mode, fixed cells were air dried prior to OPTIR imaging experiments.

The spectral resolution was evaluated in a representative spectra collected in a lipid deposit of a fixed adipocyte cell (Fig. 3a). All peaks in the adipocyte OPTIR spectra could be assigned. All bands, except the peaks at 1655 cm^{-1} and 1541 cm^{-1}, the amide-I and amide-II bands, respectively[10], were assigned to lipid vibrational modes.[19,31–33] Notably, the position of the ester carbonyl vibrational mode at 1747 cm^{-1} indicates that the bulk of the lipids present are triglycerides, as expected for adipocytes.

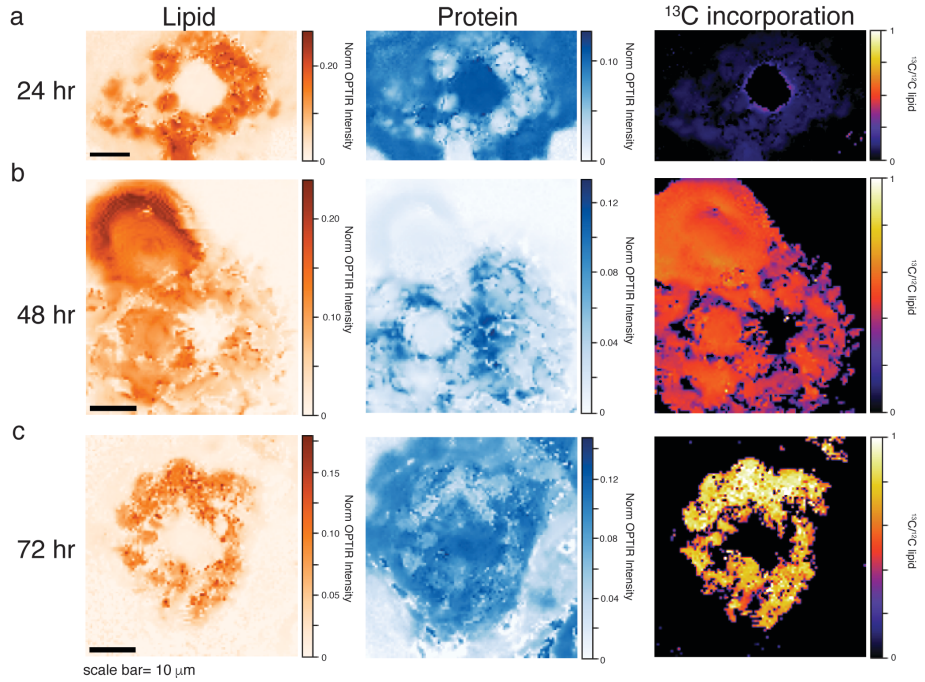

Figure 4. Changes in lipid composition over time showcase rates of DNL. Images generated from the vector normalized and average intensity of ^{12}C lipid (1737-1757 cm^{-1}) (orange), protein (1625-1700 cm^{-1}) (blue) and ratio images created from the amide-I corrected ratio of $^{13}C/^{12}C$ lipids (far right) at (a) 24, (b) 48, and (c) 72 hours after feeding cells with ^{13}C glucose. A threshold was applied so that only areas with a lipid signal above 0.025 were used for calculating the lipid ratios. Experiments were repeated three times with similar results.

To track glucose metabolism and DNL, ^{13}C glucose was fed to cells in place of ^{12}C glucose. Because the frequency of the vibrational modes of molecules has an inverse relationship with the reduced mass of the atoms involved, substituting heavier isotopes cause red-shifts in the frequency of the modes.[34,35] Glucose is the primary carbon source for generation of FFA and triglycerides in adipocytes like 3T3-L1.[36] Incorporation of the ^{13}C into lipid molecules results in significant shifts across the lipid spectra (Fig.

3b).[11,37] The most obvious is the ~44 cm^{-1} red shift of the ^{13}C ester carbonyl stretch as compared to the ^{12}C ester carbonyl stretch. As the single strongest lipid vibrational mode, the ester carbonyl stretch is an excellent probe of lipids within the cell. By calculating the ratio of the ester ^{13}C=O band to the ester ^{12}C=O over time, the rate of DNL can be tracked.[11]

OPTIR provides high resolution hyperspectral imaging. The spatial resolution of OPTIR is determined by the diffraction limit of the 532 nm probe laser. Line scans using 500 nm spacing confirmed the manufacturer specifications; OPTIR has a spatial resolution of 500 nm.[24] Hyperspectral maps are three-dimensional images assembled from complete OPTIR spectra, 801-1799 cm^{-1}, collected at every point. All hyperspectral maps were collected using 500 nm spacing.

Noticeably, as compared to the appearance of living adipocytes, fixed, dried cells experienced some pooling and combining of the lipid droplets into deposits. This has been previously reported and does not affect the lipid spectra, but does affect lipid distribution and overlap with protein signal.[32] We chose not to use a post-fixative agent on the lipids as we did not wish to introduce additional vibrationally active chemicals or cause changes to lipid molecular structure. Nevertheless, disruption of lipid droplet morphology is a significant drawback of fixed, dried cells and highlights the importance of live cell data collection for properly imaging lipid localization.

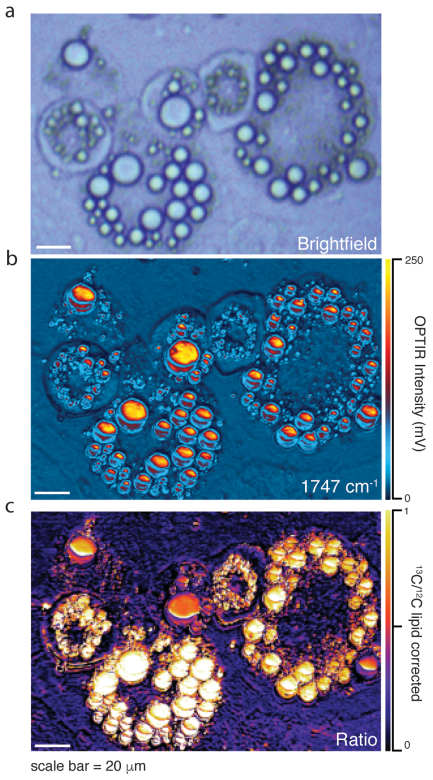

Figure 5. Visualization of rates of DNL in live adipocytes. Live differentiated 3T3-L1 adipocytes 72 hours after feeding with ^{13}C glucose. (a) Brightfield image. (b) Single wavenumber image collected at 1747 cm^{-1} corresponding with ^{12}C lipid ester carbonyl band. (c) Ratio image showing ^{13}C lipid ester carbonyl (1703 cm^{-1})/ ^{12}C lipid ester carbonyl (1747 cm^{-1}) after correction for amide-I and water bending band highlighting varying rates of DNL across the cell. Data collected in PBS.

Spatiotemporal resolution of DNL in fixed cells. To track DNL, hyperspectral maps of dried, fixed cells at 24, 48, and 72 hour time points after the addition of ^{13}C glucose were collected (Fig. 4). All cells had a similar appearance with collections of lipid droplets and deposits that could be visualized by the intensity of the ^{12}C carbonyl ester band, and protein signal throughout the rest of the cell, visualized via the intensity of the amide-I band.

Ratio images of the ester ^{13}C=O band to the ester ^{12}C=O map DNL were constructed to quantify DNL in each cell (Fig. 4 ^{13}C incorporation). The images were assessed in two ways, as a single-cell average of the lipid rich areas or with full spatial resolution over the lipid rich areas. We chose only to analyze the regions with significant lipid signal to reduce noise in lipid free areas that may be amplified by creating ratio images. We found that the average single-cell $^{13}C/^{12}C$ ratio continually increased over the period of time tested (72 hours) with a final ratio of 0.54 ± 0.14. The data broadly agrees with two past studies that tracked DNL via heavy isotope incorporation into triglycerides. Shi *et al.* used QCL-based FTIR imaging to obtain ratios of ^{13}C lipid ester carbonyl/ ^{12}C lipid ester carbonyl in 3T3-L1 MBX cells at 72 h with low spatial resolution. They did not report any average data, however, the ^{13}C lipid ester carbonyl/ ^{12}C lipid ester carbonyl ratio range reported in their cell images (ratios between 0.1 – 0.7) agrees with the ranges we see. Our measurements are also in line with DNL rates reported for PANC1 pancreatic cancer cells; Li and Cheng reported end points of DNL at 72 h (a ratio of ~0.6) via a ratio of the lipid C-D/ lipid C-H as measured by single frequency SRS imaging.[4,17] Normal immortalized epithelial cells and prostate cancer cell lines, LNCaP and PC3, had significantly lower ratio end points.[4] To meet increased energy needs, cancer cells rely on metabolic rewiring such as upregulation of DNL.[1] It is intriguing that a similar rate of DNL is observed in 3T3-L1

adipocyte and PANC1 pancreatic cancer cells, as it suggests that DNL is so upregulated in this particular cancer cell line that it is in line with adipocytes.

In line with the single-cell average data, as time progressed the ratio of $^{13}C{=}O/^{12}C{=}O$ labeled lipids within the cell increased in the ratio image (Fig. 4 ^{13}C incorporation). Highlighting the importance of considering spatial data, there was some variation in the ratio across lipid-rich regions of individual cells. In particular, the edges of lipid droplets and deposits have a lower ratio of ^{13}C labeling, especially at later time points (Fig. 4c), suggesting the presence of older lipids or slower DNL in these locations. However, it is difficult to draw strong conclusions about the spatial heterogeneity of DNL from ratio images as the shape and structure of lipid droplets is not well-preserved during fixing and drying.

Live cell imaging highlights spatiotemporal DNL heterogeneity. Although fixed, dried cells are advantageous because they enable the long imaging times necessary for collection of highly detailed hyperspectral maps, they also come with several drawbacks. Dried cells can be damaged by IR and visible lasers and drying may introduce artifacts.[18] More importantly, the fixing and drying process causes disruptions in the lipid droplets and possibly in protein structure and localization.[16,32] Loss of water can disturb organelles and change the shape and thickness of the cell, compromising the quality of spatial data.[16] Therefore, comparing against live cell data is critical to confirm observations made in fixed cells as well as tracking processes of interest in real time. Unfortunately, collecting data from hydrated samples has been nearly impossible using conventional FTIR microscopes as water is a strong IR absorber.[15] OPTIR, however, has significantly less contribution from bulk water.[20] This allows for data collection within live cells.[20]

Adipocytes at 72 hours after ^{13}C glucose feeding were mounted on slides in PBS with a 5 μm spacer to preserve hydration and minimize cell compression. In the current configuration, hyperspectral maps could not be collected because of the long imaging times, however single point full OPTIR spectra could be collected and frequencies of interest determined . Single wavenumber images of single cells were collected at 1747 cm^{-1} (ester $^{12}C{=}O$) , 1703 cm^{-1} (ester $^{13}C{=}O$), and 1655 cm^{-1} (water and amide-I bands).

Brightfield images of the live adipocyte cells show distinct lipid droplets and morphology in agreement with literature (Fig. 5a).[30] The 1747 cm^{-1} images clearly show strong lipid signals in the droplets with no lipid signal in the rest of the cell (Fig. 5b). The ratio images show varied rates of DNL, especially between cells (Fig. 5c). There is, however, some variation between lipid droplets within cells and even across lipid droplets. This hints at the complexity of glucose anabolism into lipids and lipolysis and demonstrate that this technique can detect even small differences in the ratio of ^{13}C triglycerides to ^{12}C triglycerides in living cells. Other than the shape of the lipid droplets, the data is in good agreement with the fixed cell ratios at 72 h with the $^{13}C/^{12}C$ lipid ester carbonyl ratio varying from ~0.4 to ~1 in both cases.

Single spectra were collected to compare with fixed cells. Full spectra show good agreement with fixed cell data and similar ratios between the ^{13}C and ^{12}C ester carbonyls at the 72 h time point (Fig. 6). The lipid droplets were better defined in spectral images of live cells than in fixed cells and had less overlap with protein amide-I signal, as seen by full spectra (Fig. 6). While the vibrational mode of water at ~1645 cm^{-1} could obscure the amide-I mode, the absence of proteins in the lipid droplets is confirmed by the absence of the amide-II band (Fig. 6).[10,15] This data implies that fixed cells provide reliable data on the range of rates of DNL seen across the cell. Unfortunately, the collapse of the lipid

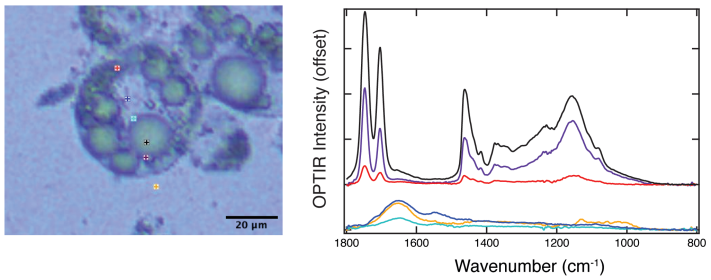

Figure 6. Full OPTIR spectra collected in hydrated, living adipocytes. Live differentiated 3T3-L1 adipocytes 72 hours after feeding with ^{13}C glucose. Brightfield (left) with points spectra were collected from indicated. Colors match corresponding full OPTIR spectra (right). Black, purple, and red spectra, which represent lipid rich regions, are offset.

droplets in fixed cells causes protein and lipid signals to overlap, which does not occur to a significant extent in the live cells. This may obscure signal from the lipids and also means that it is impossible to comment on lipid localization in the fixed cells. Therefore, for questions in which high resolution spatial information is needed, live cells should be used. Fixed cells, however, are suitable for hyperspectral imaging, which can provide information on lipid species occurring at lower concentrations, like FFA, and allow complete analysis of lipid and protein spectral features at each location. This work demonstrates that OPTIR is suitable for live and fixed cell analysis and that IR probes can be simply incorporated and then identified by OPTIR. It thus lays the groundwork for my proposed research.

Proposed Research

Aim 1. Characterize rates of DNL across cell lines and changes in response to stress and drugs

Dysfunction in DNL has been linked to a variety of diseases, including obesity, cancer, and several viral infections.[29] Most notably, hepatic DNL elevation is a hallmark of non-alcoholic fatty liver disease (NAFLD), a disease with a lifetime prevalence above 25%![38] Understanding basal rates of DNL across cell lines and how it changes in response to stressors and drugs is critical for a better understanding of the disease and testing the effects of drugs that target DNL or tracking DNL in an individual to predict disease onset and severity. My preliminary work has shown that OPTIR is an excellent technique for tracking DNL in both living and fixed cells. In adipocytes there were significant variations in the incorporation of ^{13}C into the triglycerides between cells. The large standard deviation in the average ratios highlights cell to cell difference in average rates of DNL (Fig. 7a). DNL is also spatially heterogenous; at 72 h, histograms of the $^{13}C/^{12}C$ ratios measured in lipid rich regions of single cells vary from 0 to above 1, indicating that the local ^{13}C enrichment ranges from 0 to well above 50% (Fig. 7b-d). This intra and intercellular variation will be characterized in additional cell lines.

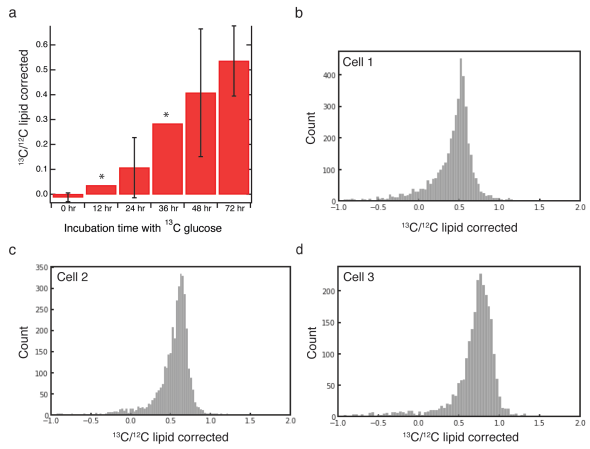

Figure 7. Increasing ratio of ^{13}C labeled lipid over time. (a) Average ratio of ^{13}C:^{12}C lipid as calculated by eq. 1 of lipid rich regions of cell (n = 3 cells where error bars shown, * = only one cell measured for these time points). Between 1000 and 6000 spectra made up the lipid rich regions of each cell. (b-d) Histograms of ^{13}C:^{12}C lipid ratios for three cells at 72 hours after addition on ^{13}C glucose, demonstrating inter and intra-cellular spread.

1.1 Optimize DNL rate measurements for Huh-7 cells. First, I will culture Huh-7 liver cells and replace the ^{12}C glucose with ^{13}C labeled glucose for 1-4 days. Cells will be imaged fixed and live as previously described for 3T3-L1 cells. I will ensure that the much smaller lipid droplets are able to be observed in the hepatic cells and that ^{13}C glucose uptake and processing happens on a reasonable time scale (hours to days). DNL rates will be calculated for the cells under normal conditions.

1.2 Design flow cell for real-time observation of drugs and stress on living cells. One of the benefits of OPTIR is its ability to collect high-resolution data inside of living cells. This allows for observation of how metabolic processes change in real-time. The addition of a flow cell would allow for the introduction of drugs, stressors, and other stimuli during observation of the Huh-7 cells to track the reaction of the DNL pathway on a sub-minute timescale. We have prototyped several flow cells, but I will work to improve the set up to allow for heating (to keep cells at 37 ºC or apply heat stress) and easy removal of both windows for cleaning of the calcium fluoride, an expensive but necessary substrate that must be carefully decontaminated and cleaned to remove biohazards and remain transparent in the infrared region. Additionally, as ^{13}C incorporation into lipids does not become obvious to the naked eye in the spectra for

several hours, analysis software based in Python or MATLAB may need to be developed to detect earlier changes. Once the flow cell is constructed it will be tested by switching Huh-7 cells into isotopically labelled glucose media using it and measuring DNL in real time.

1.3 Map basal DNL levels across cancer cells. DNL rates will be mapped across cancer cell lines in which glycolysis and DNL are suspected or known to be upregulated.[29] This includes breast cancer cell lines MCF-7 and T47D[39], prostate cancer cell lines PC-3 and LNCaP[12,32,40], lung cancer cell lines A549 and H460[41], and colorectal cancer cell lines HT29 and SW480[42]. Currently, there is little to no data on differences in spatial organization of DNL across cell lines. I will work to build a library of this information. DNL rate will be recorded as the ratio between ^{13}C and ^{12}C labelled lipids with both average data across the cell (Fig. 7a), images (Fig. 4), and histograms of the ratio at all lipid rich points (Fig. 7b-d) to capture heterogeneity between and across cells.

1.4 Measure the effects of drugs and stress on DNL. Drugs known to be direct inhibitors of enzymes involved in glycolysis and fatty acid synthesis such as benzenetricarboxylate[43] will be applied to the tissues to see how they affect DNL rate and cell survival across cell lines with a particular eye towards those with the highest rates of DNL. Additionally, various stress and disease like conditions will be tested. This will lay the foundation for a pipeline of testing DNL directed anti-cancer treatments.

Aim 2. Discern the changes in structure of phosphofructokinase (PFK) upon binding of allosteric effectors *in vitro* and *in cellulo*

DNL begins with glycolysis and the spatial organization of metabolic enzymes crucial to glycolysis is an area of great research interest. Reorganization of metabolic enzymes appears to be a critical stress response in the cell.[2,44,45] Phosphofructokinase (PFK) is a glycolytic enzyme that performs the committing step of glycolysis. In humans, there are three PFK isoforms, liver (PFKL), muscle (PFKM), and platelet (PFKP), that occur in varying ratios depending on the tissue type. PFKL has been shown to both enter G bodies and form separate phase separated structures in cells[46] and *C. elegans*[47] during nutrient stress, overexpression, and addition of activators and inhibitors. How this mechanism is triggered and regulated is not well understood. It may serve a storage depot for inactivated enzyme or a concentrated pool of glycolytic activity or both, as this condensation forms in response to both inhibition and activation. Additionally, the ability of PFKL to form higher-order oligomers *in vitro* has been known for many years (Fig. 8).[45] Recently, it was demonstrated that in high substrate conditions *in vitro*, PFKL forms filaments composed of stacked tetramers.[46] In order to understand the connection between in cell puncta and filamentation, if there is one, conditions that induce both must be fully understood and structures mapped.

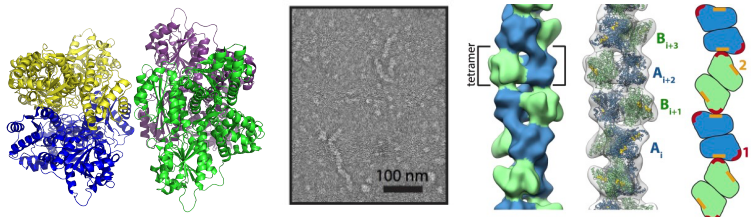

Figure 8. (a) Crystal Structure of PFKL tetramer PDB: 4WL0 (b) Transmission electron microscopy image and (c) model of PFKL filaments after saturation with fructose-6-phosphate. Adapted from ref. 46.

2.1 Express and purify high quality PFK. First, the three isoforms of PFK will be expressed in *E. coli* deficient in their own PFK homolog, strain RL257.[48] Ideally, pDream vectors will be used so the same construct can also be transfected in mammalian systems, but as human PFK has proven difficult to express in *E. coli*, bacteria optimized sequences encoded on pet28b vectors may be necessary.[49] A C-terminal 6x histidine tag preceded by a thrombin cleavage sequence will be included to aid in purification. Nickel-affinity chromatography will be used for purification, followed by cleavage of the histidine tag. PFK purification will be validated by SDS-PAGE, liquid chromatography mass spectrometry, circular dichroism temperature melts, and activity assays.

2.2 Evaluate PFK isoform structures in solution and following filamentation. The proteins will be evaluated in solution by OPTIR, FTIR (for instrument validation), and circular dichroism (CD) to obtain a structural baseline. The amide-I will be analyzed via multipeak fitting and second derivative analysis to assess various secondary structure components' contribution. PFKL will then be induced to form filaments by the addition of high concentrations of its substrate, fructose-6-phosphate, and structural information collected on these via OPTIR and FTIR (solids are not suitable for CD). Although it has not been reported in the literature, we will attempt to induce filamentation of the other isoforms as well. Additionally, varied salt, polyethylene glycol (cellular crowding mimic), temperature, and the known allosteric effectors of PFK will be used to observe if LLPS can be induced *in vitro*.[2] We predict that in the right conditions all isoforms will filament and phase-separate. If PFKM or PFKP can form filaments or if any of the isoforms can form LLPS, they will be structurally characterized using OPTIR to examine the secondary structure make-up. The structural information collected will serve as a library for comparison of the in-cell data. Any filaments formed will also be characterized by electron microscopy. We expect that filaments formed in different conditions (i.e. allosteric inhibition vs. activation) will have different structures with distinct OPTIR spectra. This may explain why and how LLPS forms in response to very different cellular stimuli.

2.3 Test conditions on cells to induce LLPS. I will test the various allosteric effectors and stress conditions on Huh-7 human liver cells transfected with fluorescently tagged PFK isoforms and assess for puncta formation. Allosteric effectors include citrate, ATP, AMP, ADP and stress conditions include general nutrient stress, glucose deficiency, and hypoxia. Conditions that form robust puncta in short time frames will be used in Aim 3. PFKL is expected to form puncta in most conditions. PFKM and PFKP are not expected to form puncta in any conditions, although any conditions that cause *in vitro* phase separation or filamentation may also induce *in cellulo* LLPS.

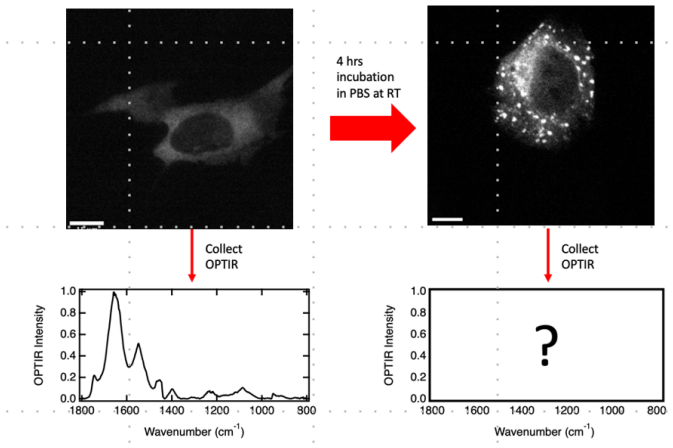

Figure 9. Schematic for collection of structural information in cells during cellular stress. Scale bar is 15 μm. Data collected by Vincent Chang.

Aim 3. Aim 3 Connect *in vitro* structures to *in cellulo* condensates

In order to understand if this higher order oligomerization is occurring in cells and identify the structures therein, a spatially and temporally resolved technique that can provide structural information resolvable from the cellular background is needed. Further, the structural information gained in even normal conditions can help to improve and validate *in vitro* structures, as the cellular milieu can have significant effects on protein structure.[50] OPTIR can bridge the gap between *in vitro* structures and the cell. We hypothesize that structures characterized in cells of PFK will be similar, but not identical to *in vitro* structures, and that visually identical condensates formed in the presence of different allosteric activators or inhibitors will have distinguishable structures.

3.1 Map basal and high puncta forming conditions with OPTIR. Fluorescently labeled PFKL will be transfected into Huh-7 liver cells. Cells will be mapped with OPTIR to see if overexpression is apparent in cellular amide-I signal and to obtain a basal background in normal and overexpressed conditions. PFK structural information will be obtained by subtracting spectra from untransfected control cells and then analyzing the amide-I bands. The cells will then be subjected to a stress or allosteric effector found to form robust puncta during Aim 2. These labeled puncta will be mapped with OPTIR to identify structures (Fig. 9). It is likely that the structure of the fluorescent tags (β-barrel of fluorescent protein) will obscure PFKL structure, but visualizing this alone will be excellent proof of concept.

3.2 Move to tag-free or almost tag-free conditions. First fluorescently tagged protein will be used to simplify puncta identification, but the puncta should be identifiable via amide-I shifts in the IR imaging, so tag-free imaging will be the goal. OPTIR will be used to gain structural information from inside the puncta. This will be compared to the *in vitro* results. We predict that there will be significant structural similarity between the *in vitro* filaments and the *in cellulo* puncta. PFKL will also be exposed to each allosteric effector and various forms of cellular stress to see if this impacts structure inside the puncta.

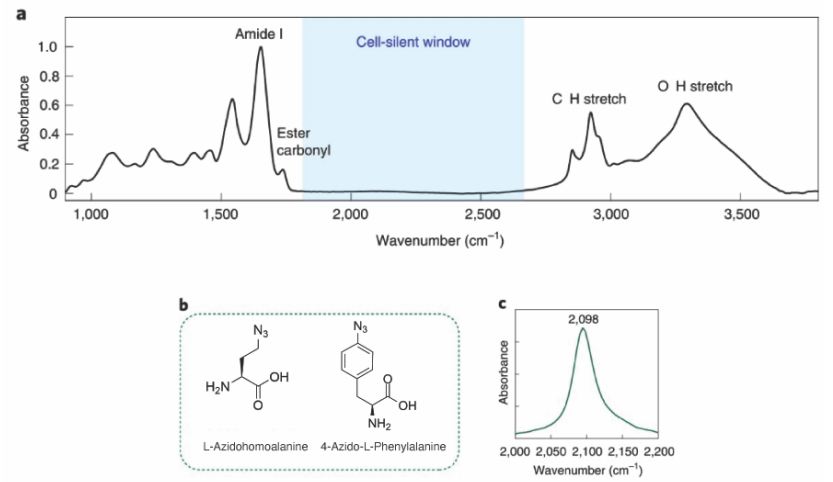

Figure 10. Azide probes in the cell-silent window. (a) Full IR spectra of a cell, showing region with no naturally occurring vibrational modes, (b) chemical structures of two azide modified amino acid probes, and (c) the IR absorbance of an azide group in the cell-silent region. Adapted from ref. 11.

Although others have successfully assigned structural elements of the amide-I in OPTIR spectra to overexpressed proteins[28], resolving phase-separated structures or locating PFK without labels may be difficult. In this case, PFK will be expressed in the cells with an azide probe (Fig. 10).[51] Amber codon technology can replace one or more residues with an azido group containing analog and allow direct expression of an azide tagged protein.[52] Data suggests this will not impact enzyme activity.[53] Triple bonds are uncommon in nature and have a unique vibrational mode far-removed from all cellular signals (Fig. 10a,c).[51] By imaging a cell at the azide vibrational mode, the location of the tagged protein can be easily identified and the amide-I can be examined for structural information. Further, the absorbance of the probe is sensitive to the local environment, providing site-specific information. If locating PFK still proved difficult, the azide probes could be uniformly incorporated for greater concentration and therefore signal.

3.3 More native stress conditions. Assuming data is successfully collected inside of Huh-7 cells, PFKL will be transfected in THP-1 cells that have been differentiated into both the inflammatory and anti-inflammatory subtypes.[54] The inflammatory subtype has elevated citrate and increased cellular stressors, allowing for a more biologically relevant test of the effects of allosteric effectors and cellular stress on PFKL. OPTIR will be used to assess PFKL secondary structure in the two cell subtypes. This is particularly biologically relevant as PFKL is the dominant isoform in immune cells like THP-1.[55]

Conclusions

This work aims to understand how the cell organizes its complex metabolism and in particular how that organization adapts to stress and disease. Recent work has demonstrated that phase separation and filamentation of enzymes and other biomolecules is conserved mechanism used across the cell in multiple metabolic processes.[2,44,45] OPTIR is a promising technique in this domain as it is compatible with living systems and can resolve molecular identity and protein structure with high resolution in space and time. This proposal focuses on DNL and a small part of glycolysis, but the technique can be used for almost any biological or metabolic process and this can help lay the foundation for label free imaging with high resolution in space and time and a better understanding of how the cell meets its energy needs in a changing environment.

References

(1) Voit, E. O. The Best Models of Metabolism. *WIREs Syst. Biol. Med.* **2017**, *9* (6), e1391. https://doi.org/10.1002/wsbm.1391.

(2) Boeynaems, S.; Alberti, S.; Fawzi, N. L.; Mittag, T.; Polymenidou, M.; Rousseau, F.; Schymkowitz, J.; Shorter, J.; Wolozin, B.; Bosch, L. V. D.; Tompa, P.; Fuxreiter, M. Protein Phase Separation: A New Phase in Cell Biology. *Trends Cell Biol.* **2018**, *28* (6), 420–435. https://doi.org/10.1016/j.tcb.2018.02.004.

(3) Jin, M.; Fuller, G. G.; Han, T.; Yao, Y.; Alessi, A. F.; Freeberg, M. A.; Roach, N. P.; Moresco, J. J.; Karnovsky, A.; Baba, M.; Yates, J. R.; Gitler, A. D.; Inoki, K.; Klionsky, D. J.; Kim, J. K. Glycolytic Enzymes Coalesce in G Bodies under Hypoxic Stress. *Cell Rep.* **2017**, *20* (4), 895–908. https://doi.org/10.1016/j.celrep.2017.06.082.

(4) Metallo, C. M.; Walther, J. L.; Stephanopoulos, G. Evaluation of 13C Isotopic Tracers for Metabolic Flux Analysis in Mammalian Cells. *J. Biotechnol.* **2009**, *144* (3), 167–174. https://doi.org/10.1016/j.jbiotec.2009.07.010.

(5) Metallo, C. M.; Gameiro, P. A.; Bell, E. L.; Mattaini, K. R.; Yang, J.; Hiller, K.; Jewell, C. M.; Johnson, Z. R.; Irvine, D. J.; Guarente, L.; Kelleher, J. K.; Vander Heiden, M. G.; Iliopoulos, O.; Stephanopoulos, G. Reductive Glutamine Metabolism by IDH1 Mediates Lipogenesis under Hypoxia. *Nature* **2012**, *481* (7381), 380–384. https://doi.org/10.1038/nature10602.

(6) Matthäus, C.; Bird, B.; Miljković, M.; Chernenko, T.; Romeo, M.; Diem, M. Infrared and Raman Microscopy in Cell Biology. *Methods Cell Biol.* **2008**, *89*, 275–308. https://doi.org/10.1016/S0091-679X(08)00610-9.

(7) Naumann, D. Infrared Spectroscopy of Cells, Tissues, and Biofluids. In *Encyclopedia of Biophysics*; Roberts, G. C. K., Ed.; Springer: Berlin, Heidelberg, 2013; pp 1057–1065. https://doi.org/10.1007/978-3-642-16712-6_120.

(8) Romeo, M. J.; Boydston-White, S.; Matthäus, C.; Miljković, M.; Bird, B.; Chernenko, T.; Diem, M. Vibrational Microspectroscopy of Cells and Tissues. In *Biomedical Vibrational Spectroscopy*; John Wiley & Sons, Ltd, 2008; pp 121–152. https://doi.org/10.1002/9780470283172.ch6.

(9) Diem, M.; Romeo, M.; Boydston-White, S.; Miljkovic, M.; Matthaus, C. A Decade of Vibrational Micro-Spectroscopy of Human Cells and Tissue (1994-2004). *The Analyst* **2004**, *129* (10), 880–885. https://doi.org/10.1039/b408952a.

(10) Barth, A. Infrared Spectroscopy of Proteins. *Biochim. Biophys. Acta BBA - Bioenerg.* **2007**, *1767* (9), 1073–1101. https://doi.org/10.1016/j.bbabio.2007.06.004.

(11) Shi, L.; Liu, X.; Shi, L.; Stinson, H. T.; Rowlette, J.; Kahl, L. J.; Evans, C. R.; Zheng, C.; Dietrich, L. E. P.; Min, W. Mid-Infrared Metabolic Imaging with Vibrational Probes. *Nat. Methods* **2020**, *17* (8), 844–851. https://doi.org/10.1038/s41592-020-0883-z.

(12) Li, J.; Cheng, J.-X. Direct Visualization of De Novo Lipogenesis in Single Living Cells. *Sci. Rep.* **2014**, *4* (1), 6807. https://doi.org/10.1038/srep06807.

(13) Centrone, A. Infrared Imaging and Spectroscopy Beyond the Diffraction Limit. *Annu. Rev. Anal. Chem.* **2015**, *8* (1), 101–126. https://doi.org/10.1146/annurev-anchem-071114-040435.

(14) Yang, H.; Yang, S.; Kong, J.; Dong, A.; Yu, S. Obtaining Information about Protein Secondary Structures in Aqueous Solution Using Fourier Transform IR Spectroscopy. *Nat. Protoc.* **2015**, *10* (3), 382–396. https://doi.org/10.1038/nprot.2015.024.

(15) Venyaminov SYu, null; Prendergast, F. G. Water (H2O and D2O) Molar Absorptivity in the 1000-4000 Cm-1 Range and Quantitative Infrared Spectroscopy of Aqueous Solutions. *Anal. Biochem.* **1997**, *248* (2), 234–245. https://doi.org/10.1006/abio.1997.2136.

(16) Lyng, F.; Gazi, E.; Gardner, P. Preparation of Tissues and Cells for Infrared and Raman Spectroscopy and Imaging; Technological University Dublin, 2011. https://doi.org/10.21427/KWG8-F843.

(17) Hobro, A. J.; Smith, N. I. An Evaluation of Fixation Methods: Spatial and Compositional Cellular Changes Observed by Raman Imaging. *Vib. Spectrosc.* **2017**, *91*, 31–45. https://doi.org/10.1016/j.vibspec.2016.10.012.

(18) Mohlenhoff, B.; Romeo, M.; Diem, M.; Wood, B. R. Mie-Type Scattering and Non-Beer-Lambert Absorption Behavior of Human Cells in Infrared Microspectroscopy. *Biophys. J.* **2005**, *88* (5), 3635–3640. https://doi.org/10.1529/biophysj.104.057950.

(19) Bik, E.; Ishigaki, M.; Blat, A.; Jasztal, A.; Ozaki, Y.; Malek, K.; Baranska, M. Lipid Droplet Composition Varies Based on Medaka Fish Eggs Development as Revealed by NIR-, MIR-, and Raman Imaging. *Molecules* **2020**, *25* (4), 817. https://doi.org/10.3390/molecules25040817.

(20) Spadea, A.; Denbigh, J.; Lawrence, M. J.; Kansiz, M.; Gardner, P. Analysis of Fixed and Live Single Cells Using Optical Photothermal Infrared with Concomitant Raman Spectroscopy. *Anal. Chem.* **2021**, *93* (8), 3938–3950. https://doi.org/10.1021/acs.analchem.0c04846.

(21) Zarei, A.; Klumbach, S.; Keppler, H. The Relative Raman Scattering Cross Sections of H2O and D2O, with Implications for In Situ Studies of Isotope Fractionation. *ACS Earth Space Chem.* **2018**, *2* (9), 925–934. https://doi.org/10.1021/acsearthspacechem.8b00078.

(22) Kuhar, N.; Sil, S.; Verma, T.; Umapathy, S. Challenges in Application of Raman Spectroscopy to Biology and Materials. *RSC Adv.* **2018**, *8* (46), 25888–25908. https://doi.org/10.1039/C8RA04491K.

(23) Reffner, J. Advances in Infrared Microspectroscopy and Mapping Molecular Chemical Composition at Submicrometer Spatial Resolution. *Spectroscopy* **2018**, *33* (9), 12–17.

(24) Zhang, D.; Li, C.; Zhang, C.; Slipchenko, M. N.; Eakins, G.; Cheng, J.-X. Depth-Resolved Mid-Infrared Photothermal Imaging of Living Cells and Organisms with Submicrometer Spatial Resolution. *Sci. Adv.* **2016**, *2* (9), e1600521. https://doi.org/10.1126/sciadv.1600521.
(25) Kansiz, M.; Prater, C.; Dillon, E.; Lo, M.; Anderson, J.; Marcott, C.; Demissie, A.; Chen, Y.; Kunkel, G. Optical Photothermal Infrared Microspectroscopy with Simultaneous Raman – A New Non-Contact Failure Analysis Technique for Identification of <10 Mm Organic Contamination in the Hard Drive and Other Electronics Industries. *Microsc. Today* **2020**, *28* (3), 26–36. https://doi.org/10.1017/s1551929520000917.
(26) Zhang, D.; Li, C.; Zhang, C.; Slipchenko, M. N.; Eakins, G.; Cheng, J.-X. Depth-Resolved Mid-Infrared Photothermal Imaging of Living Cells and Organisms with Submicrometer Spatial Resolution. *Sci. Adv.* **2016**, *2* (9), e1600521. https://doi.org/10.1126/sciadv.1600521.
(27) Lipson, S. G.; Lipson, H.; Tannhauser, D. S. *Optical Physics*; Cambridge University Press, 1995.
(28) Klementieva, O.; Sandt, C.; Martinsson, I.; Kansiz, M.; Gouras, G. K.; Borondics, F. Super-Resolution Infrared Imaging of Polymorphic Amyloid Aggregates Directly in Neurons. *Adv. Sci.* **2020**, *7* (6), 1903004. https://doi.org/10.1002/advs.201903004.
(29) Ameer, F.; Scandiuzzi, L.; Hasnain, S.; Kalbacher, H.; Zaidi, N. De Novo Lipogenesis in Health and Disease. *Metab. - Clin. Exp.* **2014**, *63* (7), 895–902. https://doi.org/10.1016/j.metabol.2014.04.003.
(30) Zebisch, K.; Voigt, V.; Wabitsch, M.; Brandsch, M. Protocol for Effective Differentiation of 3T3-L1 Cells to Adipocytes. *Anal. Biochem.* **2012**, *425* (1), 88–90. https://doi.org/10.1016/j.ab.2012.03.005.
(31) Derenne, A.; Claessens, T.; Conus, C.; Goormaghtigh, E. Infrared Spectroscopy of Membrane Lipids. In *Encyclopedia of Biophysics*; Roberts, G. C. K., Ed.; Springer: Berlin, Heidelberg, 2013; pp 1074–1081. https://doi.org/10.1007/978-3-642-16712-6_558.
(32) Gazi, E.; Gardner, P.; Lockyer, N. P.; Hart, C. A.; Brown, M. D.; Clarke, N. W. Direct Evidence of Lipid Translocation between Adipocytes and Prostate Cancer Cells with Imaging FTIR Microspectroscopy. *J. Lipid Res.* **2007**, *48* (8), 1846–1856. https://doi.org/10.1194/jlr.M700131-JLR200.
(33) Rak, S.; Zan, T. D.; Stefulj, J.; Kosović, M.; Gamulin, O.; Osmak, M. FTIR Spectroscopy Reveals Lipid Droplets in Drug Resistant Laryngeal Carcinoma Cells through Detection of Increased Ester Vibrational Bands Intensity. *Analyst* **2014**, *139* (13), 3407–3415. https://doi.org/10.1039/C4AN00412D.
(34) Marecek, J.; Song, B.; Brewer, S.; Belyea, J.; Dyer, R. B.; Raleigh, D. P. A Simple and Economical Method for the Production of 13C,18O-Labeled Fmoc-Amino Acids with High Levels of Enrichment: Applications to Isotope-Edited IR Studies of Proteins. *Org. Lett.* **2007**, *9* (24), 4935–4937. https://doi.org/10.1021/ol701913p.
(35) Tadesse, L.; Nazarbaghi, R.; Walters, L. Isotopically Enhanced Infrared Spectroscopy: A Novel Method for Examining Secondary Structure at Specific Sites in Conformationally Heterogeneous Peptides. *J. Am. Chem. Soc.* **1991**, *113* (18), 7036–7037. https://doi.org/10.1021/ja00018a052.
(36) Collins, J. M.; Neville, M. J.; Pinnick, K. E.; Hodson, L.; Ruyter, B.; van Dijk, T. H.; Reijngoud, D.-J.; Fielding, M. D.; Frayn, K. N. De Novo Lipogenesis in the Differentiating Human Adipocyte Can Provide All Fatty Acids Necessary for Maturation. *J. Lipid Res.* **2011**, *52* (9), 1683–1692. https://doi.org/10.1194/jlr.M012195.
(37) Muhamadali, H.; Chisanga, M.; Subaihi, A.; Goodacre, R. Combining Raman and FT-IR Spectroscopy with Quantitative Isotopic Labeling for Differentiation of E. Coli Cells at Community and Single Cell Levels. *Anal. Chem.* **2015**, *87* (8), 4578–4586. https://doi.org/10.1021/acs.analchem.5b00892.
(38) Riazi, K.; Azhari, H.; Charette, J. H.; Underwood, F. E.; King, J. A.; Afshar, E. E.; Swain, M. G.; Congly, S. E.; Kaplan, G. G.; Shaheen, A.-A. The Prevalence and Incidence of NAFLD Worldwide: A Systematic Review and Meta-Analysis. *Lancet Gastroenterol. Hepatol.* **2022**, *7* (9), 851–861. https://doi.org/10.1016/S2468-1253(22)00165-0.
(39) Simeone, P.; Tacconi, S.; Longo, S.; Lanuti, P.; Bravaccini, S.; Pirini, F.; Ravaioli, S.; Dini, L.; Giudetti, A. M. Expanding Roles of De Novo Lipogenesis in Breast Cancer. *Int. J. Environ. Res. Public. Health* **2021**, *18* (7), 3575. https://doi.org/10.3390/ijerph18073575.
(40) Zadra, G.; Ribeiro, C. F.; Chetta, P.; Ho, Y.; Cacciatore, S.; Gao, X.; Syamala, S.; Bango, C.; Photopoulos, C.; Huang, Y.; Tyekucheva, S.; Bastos, D. C.; Tchaicha, J.; Lawney, B.; Uo, T.; D'Anello, L.; Csibi, A.; Kalekar, R.; Larimer, B.; Ellis, L.; Butler, L. M.; Morrissey, C.; McGovern, K.; Palombella, V. J.; Kutok, J. L.; Mahmood, U.; Bosari, S.; Adams, J.; Peluso, S.; Dehm, S. M.; Plymate, S. R.; Loda, M. Inhibition of de Novo Lipogenesis Targets Androgen Receptor Signaling in Castration-Resistant Prostate Cancer. *Proc. Natl. Acad. Sci. U. S. A.* **2019**, *116* (2), 631–640. https://doi.org/10.1073/pnas.1808834116.
(41) Singh, A.; Ruiz, C.; Bhalla, K.; Haley, J. A.; Li, Q. K.; Acquaah-Mensah, G.; Montal, E.; Sudini, K. R.; Skoulidis, F.; Wistuba, I. I.; Papadimitrakopoulou, V.; Heymach, J. V.; Boros, L. G.; Gabrielson, E.; Carretero, J.; Wong, K.-K.; Haley, J. D.; Biswal, S.; Girnun, G. D. De Novo Lipogenesis Represents a Therapeutic Target in Mutant Kras Non-Small Cell Lung Cancer. *FASEB J.* **2018**, *32* (12), 7018–7027. https://doi.org/10.1096/fj.201800204.
(42) Zaytseva, Y. Y.; Harris, J. W.; Mitov, M. I.; Kim, J. T.; Butterfield, D. A.; Lee, E. Y.; Weiss, H. L.; Gao, T.; Evers, B. M. Increased Expression of Fatty Acid Synthase Provides a Survival Advantage to Colorectal Cancer Cells via Upregulation of Cellular Respiration. *Oncotarget* **2015**, *6* (22), 18891–18904.

(43) Batchuluun, B.; Pinkosky, S. L.; Steinberg, G. R. Lipogenesis Inhibitors: Therapeutic Opportunities and Challenges. *Nat. Rev. Drug Discov.* **2022**, *21* (4), 283–305. https://doi.org/10.1038/s41573-021-00367-2.
(44) Prouteau, M.; Loewith, R. Regulation of Cellular Metabolism through Phase Separation of Enzymes. *Biomolecules* **2018**, *8* (4), 160. https://doi.org/10.3390/biom8040160.
(45) Park, C. K.; Horton, N. C. Structures, Functions, and Mechanisms of Filament Forming Enzymes: A Renaissance of Enzyme Filamentation. *Biophys. Rev.* **2019**, *11* (6), 927–994. https://doi.org/10.1007/s12551-019-00602-6.
(46) Webb, B. A.; Dosey, A. M.; Wittmann, T.; Kollman, J. M.; Barber, D. L. The Glycolytic Enzyme Phosphofructokinase-1 Assembles into Filaments. *J. Cell Biol.* **2017**, *216* (8), 2305–2313. https://doi.org/10.1083/jcb.201701084.
(47) Jang, S.; Xuan, Z.; Lagoy, R. C.; Jawerth, L. M.; Gonzalez, I. J.; Singh, M.; Prashad, S.; Kim, H. S.; Patel, A.; Albrecht, D. R.; Hyman, A. A.; Colón-Ramos, D. A. Phosphofructokinase Relocalizes into Subcellular Compartments with Liquid-like Properties in Vivo. *Biophys. J.* **2021**, *120* (7), 1170–1186. https://doi.org/10.1016/j.bpj.2020.08.002.
(48) Lovingshimer, M. R.; Siegele, D.; Reinhart, G. D. Construction of an Inducible, PfkA and PfkB Deficient Strain of Escherichia Coli for the Expression and Purification of Phosphofructokinase from Bacterial Sources. *Protein Expr. Purif.* **2006**, *46* (2), 475–482. https://doi.org/10.1016/j.pep.2005.09.015.
(49) *pDream2.1/MCS - GenScript*. https://www.genscript.com/vector/SD0222-pDream2_1_MCS.html?page_no=1&position_no=1&sensors=search&correct=pdream&wrong=pdrean (accessed 2021-12-06).
(50) Wirth, A. J.; Gruebele, M. Quinary Protein Structure and the Consequences of Crowding in Living Cells: Leaving the Test-Tube Behind. *BioEssays News Rev. Mol. Cell. Dev. Biol.* **2013**, *35* (11), 984–993. https://doi.org/10.1002/bies.201300080.
(51) Wei, L.; Hu, F.; Chen, Z.; Shen, Y.; Zhang, L.; Min, W. Live-Cell Bioorthogonal Chemical Imaging: Stimulated Raman Scattering Microscopy of Vibrational Probes. *Acc. Chem. Res.* **2016**, *49* (8), 1494–1502. https://doi.org/10.1021/acs.accounts.6b00210.
(52) Wals, K.; Ovaa, H. Unnatural Amino Acid Incorporation in E. Coli: Current and Future Applications in the Design of Therapeutic Proteins. *Front. Chem.* **2014**, *2*, 15. https://doi.org/10.3389/fchem.2014.00015.
(53) Park, J. S.; Burckhardt, C. J.; Lazcano, R.; Solis, L. M.; Isogai, T.; Li, L.; Chen, C. S.; Gao, B.; Minna, J. D.; Bachoo, R.; DeBerardinis, R. J.; Danuser, G. Mechanical Regulation of Glycolysis via Cytoskeleton Architecture. *Nature* **2020**, *578* (7796), 621–626. https://doi.org/10.1038/s41586-020-1998-1.
(54) Bosshart, H.; Heinzelmann, M. THP-1 Cells as a Model for Human Monocytes. *Ann. Transl. Med.* **2016**, *4* (21), 438–438. https://doi.org/10.21037/atm.2016.08.53.
(55) Amara, N.; Cooper, M. P.; Voronkova, M. A.; Webb, B. A.; Lynch, E. M.; Kollman, J. M.; Ma, T.; Yu, K.; Lai, Z.; Sangaraju, D.; Kayagaki, N.; Newton, K.; Bogyo, M.; Staben, S. T.; Dixit, V. M. Selective Activation of PFKL Suppresses the Phagocytic Oxidative Burst. *Cell* **2021**, *184* (17), 4480-4494.e15. https://doi.org/10.1016/j.cell.2021.07.004.